PCCP

Accepted Manuscript




ROYAL SOCIETY OF CHEMISTRY

www.rsc.org/pccp

# $SnO_2(\beta\text{-}Bi_2O_3)/Bi_2Sn_2O_7$ Nanohybrids Doped Pt and Pd Nanoparticles: Applications in Visible-Light Photocatalysis, Electrical Conductivity and Dye-sensitized Solar Cells

**M. Khairy, Mohamed Mokhtar Mohamed***

Benha University, Faculty of Science, Chemistry Department, Benha, Egypt

## Abstract

$Bi_2O_3$-$SnO_2$ nanocomposites formed at a nominal molar ratio of 3:1 and loaded with Pd/Pt nanoparticles synthesized by a sol gel-hydrothermal method with the aid of a template were thoroughly characterized by X-ray diffraction, TEM-EDX, $N_2$ sorptiometry, diffuse reflectance UV-Vis, FTIR, photoluminescence and electrical conductivity. It has been shown that Pd and Pt stimulate the existence of $\beta$-$Bi_2O_3$ and $SnO_2$, respectively together with the key component $Bi_2Sn_2O_7$. The Photocatalytic results indicate that the degradation of methylene blue (MB) dye on Pd/$\beta$-$Bi_2O_3$-$Bi_2Sn_2O_7$ revealed a remarkable performance as compared to Pt/$SnO_2$-$Bi_2Sn_2O_7$ and $Bi_2O_3$-$SnO_2$ samples in both UV and visible regions. The enhanced photocatalytic activity of the Pd/$\beta$-$Bi_2O_3$-$Bi_2Sn_2O_7$ nanocomposite is primarily attributed to the broad contact between $\beta$-$Bi_2O_3$ and $Bi_2Sn_2O_7$ phases those indicate high mesoporosity and hetero-junction structures resulting in separation efficacy between photo-induced electron-hole pairs. Specifically, the photosensitive $\beta$-$Bi_2O_3$ is easily excited and released electrons to be accepted by $Bi_2Sn_2O_7$ and Pd that might be deposited in the interlayer between $\beta$-$Bi_2O_3$ and $Bi_2Sn_2O_7$. The degradation mechanism of MB over Pd/$\beta$-$Bi_2O_3$-$Bi_2Sn_2O_7$ in the visible region showed that the dye degradation proceeds through evolution of $\bullet O_2^-$ and •OH radicals as evaluated using photoluminescence and free radicals trapping experiments. An insight into the electrical properties including dielectric constant and impedance of the materials indicates that Pd/$\beta$-$Bi_2O_3$-$Bi_2Sn_2O_7$ has the highest conductivity based on increasing the ionic transport and defects at $\beta$-$Bi_2O_3$/$Bi_2Sn_2O_7$ hetero-junction. This later material displayed an improved photocurrent response of higher power conversion efficiency comprised of 50% and 250% exceeding Pt/$SnO_2$-$Bi_2Sn_2O_7$ and $SnBi_3$ respectively, in dye-sensitized solar cells. Picosecond-resolved photoluminescence (PL) and polarization gated PL anisotropy measurements were combined to clarify the process of FRET from the excited Pd/$\beta$-$Bi_2O_3$-$Bi_2Sn_2O_7$ to SD N719. This indicates that the later structure is proposed as multifunctional candidate for lead as dye-sensitized solar cell, electrical material and efficient photocatalyst based on its versatile structure.

**Keywords:** Pd/β-$Bi_2O_3$-$Bi_2Sn_2O_7$, Characterization; Photocatalysis, Electrical conductivity, Dye-sensitized solar cells

*Corresponding author: mohmok2000@yahoo.com

## 1. Introduction

Metal oxides offer a higher degree of freedom compared to single metal oxides in the sense that these oxides facilitate designing nanomaterials with superior stability and lower optical band gap. In this context, tin oxide ($SnO_2$) which is extensively used in optoelectronic devices and gas sensors is hybridized with bismuth oxide ($Bi_2O_3$); used in various applications such as microelectronics and sensor technology,[1-2] to form multiphase catalysts. Bismuth oxide of unique optical and electrical properties and has many crystallographic polymorphs, among which β phase of 2.3 eV band gap energy; lower than that of α-phase (2.85 eV), has been widely explored as a visible light photocatalyst.[3-6] However, three main problems limit further applications of β-$Bi_2O_3$ in photocatalysis. First, it is a metastable phase and simply transformed to the α-phase or to bismuth carbonate during the photocatalytic reaction. Second, it has low quantum efficiency and thus offering fast recombination of the photogenerated electron-hole pairs. Finally, the $V_B$ of β-$Bi_2O_3$ is relatively negative, thus the oxidability of the photogenerated holes in the $V_B$ is relatively weak.[7–9] Accordingly, exploiting the advantages of the binary $SnO_2$-$Bi_2O_3$ mixed oxides have been considered and indeed catalyzed several reactions such as isobutene-to-methacrolein conversion[10,11], Oxidative dehydrodimerization of propylene,[12] oxidative dehydroaromatization of isobutene,[13] and oxidative coupling of methane.[14] It has also been shown that the mentioned mixed oxides are working via a key component named bismuth pyrostannate ($Bi_2Sn_2O_7$), that has also motivated other kind of applications such as gas-sensing devices.[15-16] In addition, a mixture of $SnO_2$ and $Bi_2Sn_2O_7$ displayed high catalytic activity in the total oxidation of isobutene [17] and high selectivity in sensing CO gas.[18] However, this mixed oxide suffers from lower reactivities toward photocatalytic reactions unless β-$Bi_2O_3$ and $Bi_2Sn_2O_7$ form interfaces with either one of the oxides.[19] Recently, $Bi_2Sn_2O_7$ have also been demonstrated to exhibit visible-light driven photocatalytic activity. Conversely, its limited activity was usually attributed to the decrease in surface area as well as structural defects developed while synthesis.[19] Accordingly, for improving the photocatalytic performance of β-$Bi_2O_3$ under the irradiation of visible light, the hybridization between $Bi_2Sn_2O_7$ and β-$Bi_2O_3$ of varied work function is expected to

explore new heterostructures for photocatalytic applications. Consequently, β-$Bi_2O_3$/$Bi_2Sn_2O_7$ hybrid doped with Pd showed unprecedented activity towards fluorene oxidation under UV light irradiations exceeded that of Pd/$Bi_2O_3$.[19-20] The above mentioned results highlighted the importance of $Bi_2Sn_2O_7$ in designing the efficient hybrid consisting of $SnO_2$-$Bi_2O_3$ not only in modifying the electronic structure but also as charge separator.[21] Under visible light irradiation, the $Bi_2Sn_2O_7$ nanoparticles exhibited high photocatalytic activity in the oxidization of arsenite $(AsO_3)^{3-}$ to arsenate $(AsO_4)^{3-}$.[22] Superior photocatalytic properties for rhodamine B degradation were observed for the $Bi_{2-x}La_xSn_2O_7$ ($0.0 \leq x \leq 0.20$) system in both the UV and visible regions. The pseudo first order rate constants were found to increase in lanthanum-containing compositions and the dye degradation was found to proceed via different routes under UV and visible regions.[23] Accordingly, in a way of stabilizing the β-$Bi_2O_3$ phase to be applied in visible light assisted reactions, embedding $SnO_2$ into $Bi_2O_3$ via a template technique was performed. In this study, a novel visible-light active β-$Bi_2O_3$/$Bi_2Sn_2O_7$ photocatalyst is successfully prepared by incorporating $SnO_2$ into $Bi_2O_3$ at a ratio of 1/3 using the sol gel-hydrothermal technique and loaded with Pd nanoparticles. The latter photocatalyst was compared with that composed of $SnO_2$/$Bi_2Sn_2O_7$ those stimulated based on anchoring Pt nanoparticles, and observed to enhance the visible-light activity. These catalysts were tested for methylene blue (MB) degradation via employing UV and visible-light irradiations together with evaluating reactive intermediates responsible for the dye degradation under visible-light illumination. These materials were also employed as working electrodes of a dye sensitized solar cell (DSSC) for the purpose of evaluating the electrocatalytic ability of the nanocomposites formed of Pd/$SnO_2$-$Bi_2O_3$, Pt/$SnO_2$-$Bi_2O_3$ and $SnO_2$-$Bi_2O_3$ photocatalysts. The synthesized catalysts were thoroughly characterized using X-ray diffraction, Transmission electron microscopy-EDX, UV-Vis diffuse reflectance spectroscopy, electrical conductivity, $N_2$ sorptiometry, Picosecond-resolved photoluminescence (PL) and polarization gated PL anisotropy measurements and FTIR spectrometry.

## 2. Experimental

### 2.1. Catalyst preparation

#### 2.1.1. Synthesis of Pd(Pt)/$SnO_2$-$Bi_2O_3$nanostructures

In a typical procedure, appropriate amounts of $Bi(NO_3)_3 \cdot 5H_2O$ and $Sn(NO_3)_4$ were used so as to obtain a 3:1 atomic ratio in the final product. $Bi(NO_3)_3 \cdot 5H_2O$ was first

dissolved in water containing pluronic-123 (100 ml) [Poly(ethylene glycol)-*block*-poly(propylene glycol)-*block*-poly(ethylene glycol)]; of average $M_n$~ 5800, and same for $Sn(NO_3)_4$. $Sn(NO_3)_4$ solution was poured onto the $Bi(NO_3)_3 \cdot 5H_2O$ solution under vigorous stirring. The pH adjustment to a value of 8.8 via drop-wise addition of ammonia solution (18%, v/v) was performed until complete precipitation and thus the reacting solutions were kept at 85°C under strong stirring until a gel was formed. Then, the gel was transferred into a Teflon-lined stainless autoclave (400 mL capacity) at the temperature of 140°C for 24 h via incubation in an electric oven. The system was then cooled to ambient temperature naturally. The as-prepared sample was collected and washed with distilled water and absolute ethanol several times, vacuum-dried and then calcined at 500°C for 6 h to obtain $SnO_2$-$Bi_2O_3$ nanostructures. This sample was denoted as $SnBi_3$ where 3 accounts for the atomic ratio of 3/1(Bi/Sn). Palladium nitrate [$Pd(NO_3)_2$] and sodium hexachloroplatinate [$Na_2PtCl_6$] as to obtain 2% wt loading are taken as starting material to dope the $SnBi_3$ material, which has been dissolved in distilled water forming an emulsion using a ball mill. After mixing, sodium borohydride at a concentration of 2g/100 ml was added step-wisely to the mixture for sake of Pd/Pt ions reduction. The mixture was left for one day under stirring, filtering and washing with distilled water for several times. Then, dried at 110°C for 5 h and calcined at 500°C for 6 h. The samples were denoted as $Pd/SnBi_3$ and $Pt/SnBi_3$.

### 2.2. Catalyst characterization

#### 2.2.1. X-ray diffraction

The X-ray powder diffraction patterns of various solids were carried out using a Philips 321/00 instrument. The patterns were run with Ni-filtered Cu Kα radiation ($\lambda$ = 1.541 Å) at 36 kV and 16 mA with scanning speed of 2°in $2\theta$ $min^{-1}$. The XRD phases present in the samples were identified with the help of ASTM powder data files.

#### 2.2.2. $N_2$ adsorption

The surface properties namely BET surface area, total pore volume ($V$p) and mean pore radius ($r$) were determined from $N_2$ adsorption isotherms measured at 77 K using conventional volumetric apparatus. The samples were out-gassed at 473 K for 3 h

under a reduced pressure of $10^{-5}$ Torr before starting the measurement. The total pore volume was taken from the desorption branch of the isotherm at $p/p^0$= 0.98, assuming complete pore saturation.

### 2.2.3. Ultraviolet-visible diffuse reflectance spectroscopy

Diffuse Reflectance Ultraviolet–visible spectroscopy (UV–vis DRS) of powder samples was carried out at room temperature using a Perkin Elmer Lamda-900 spectrophotometer in the range of 200–800 nm.The UV-vis spectra were processed with Microsoft Excel software, consisting of calculation of the Kubelka-Monk function, $F(R_\infty)$, which was extracted from the UV-vis DRS absorbance. The edge energy ($E_g$) for allowed transitions was determined by finding the intercept of the straight line in the low-energy rise of the plot of $[F(R_\infty)h\mathrm{V}]^2$, for the direct allowed transition, vs $h$V, where $h$V is the incident photonenergy

### 2.2.4. Transmission Electron Microscope (TEM)

TEM micrographs were measured using a Philips; model Tecani Feil2, at an accelerating voltage of 200 KV. The powder samples were put on carbon foil with a microgrid. TEM images were observed with minimum electron irradiation to prevent damage to the sample structure.The elemental compositions of the composite material were investigated by energy-dispersive X-ray attached to the TEM equipment. The average particle diameter (d) was calculated by the following formula: d = Σnidi/Σni, where ni is the number of particle diameter di in a certain range, and Σni is more than 100 particles on TEM images of the sample. Computer-assisted counting of nanoparticle images and automated image analysis based software package including KONTRON KS 400 (Zeiss-Kontron) was used.

### 2.2.5.Photoluminescence and picosecond-resolved photoluminescence spectra

PL measurements of solids were conducted at room temperature by using a He-Cd laser (370 nm) as an excitation source. For picosecond-resolved results, we have solubilized the as-prepared nanocomposites with citrate solution followed by 3 h of extensive mixing. Then, they were filtered out (by a syringe driven filter of 0.22 μmdiameter) and UV−vis optical absorption of the resulting filtrate solution was measured using Shimadzu UV-2600 spectrophotometer using a quartz cuvette of 1 cm

pathlength. The characteristic fluorescence excitation and emission spectra of citrate−nanocomposite solutions were recorded on a Jobin Yvon Model Fluoromax-3 fluorimeter. During the capturing of fluorescence micrographs, in the case of all two excitations (300 and 375 nm), excitation light powers and integration times were kept constant. Picosecond-resolved fluorescence transients were measured by using Life Specps spectrophotometer from Edinburgh Instruments, UK for 375 nm excitation (80 ps instrument response function, IRF). For 300 nm excitation, we have utilized the third harmonic laser beam of 900 nm (0.5 nJ per pulse) using a mode locked Ti-sapphire laser with an 80 MHz repetition rate (Tsunami, Spectra Physics), pumped by a 10 W Millennia (Spectra Physics) followed by a pulse-peaker (rate 8 MHz), and a third harmonic generator(Spectra Physics, model 3980).

**2.3. Measurements of photocatalytic activity**

The photocatalytic properties of the various samples were evaluated by monitoring the degradation of MB (100 mL, 20 ppm) in the presence of 100 mg catalyst at room temperature. The photooxidation experiments were performed in a photoreactor made of quartz and equipped with a specific tubular space for the UV-Vis lamps as well as a cooling jacket. A medium pressure Hg lamp (120 W) equipped with a UVA responsive to 254-400 nm; and presented strong emission lines at 325, 343, 365, 366 and 391 nm, manufactured by Vilber Lourmat, France was used as an UV light source; with an average light intensity equal 60 $mWcm^{-2}$. On the other hand, a medium Hg lamp (150 W) with a special UV cut off filter ($\lambda$ = 420 nm) offering visible light source was also used. It was placed at a specified position using a special rod in the reactor. A continuous cold water (16±1°C) supply was maintained during the experiment to control the temperature of the reaction mixture. Prior to irradiation, the catalyst and methylene blue solution were allowed to stir in the dark for 60 minutes prior to illumination to allow for adsorption of the methylene blue onto the surface of the catalyst. Aliquots of the solution were collected at different time intervals for a total of 150 minutes. Degradation of the methylene blue dye was traced by its absorption peak at 665 nm. This absorption data was used in the determination of degradation of the dye through comparison with the absorbance at a certain time as a percentage of the initial absorbance. For detecting the active species [hydroxyl radicals (•OH), superoxide radical ($^{\bullet}O_2^-$) and holes ($h^+$)] as well as their role in the photocatalytic reaction, the following scavengers were added: 1.0 mM isopropanol

(IP- a quencher of •OH), p-benzoquinone (BQ -a quencher of $^{\bullet}O_2^-$ ), and triethanolamine (TEOA -a quencher of $h^+$). The method was similar to the former photocatalytic experiments.

**2.4.Photovoltaic efficiency measurements**

The photoelectrochemical solar cell was synthesized using viscous paste of the produced $SnBi_3$, $Pd/SnBi_3$ and $Pt/SnBi_3$ samples. It was prepared by adding 1 ml of triton X-100 to 0.5 g of each sample. The colloidal solution was sprayed over the conducting glass F-doped $SnO_2$ layer (Pilkington Kappa Energy Float), of sheet resistance ~20–22 V cm. The colloidal film was fired at 673 K for 1 h. The sintered colloidal $SnBi_3$, $Pd/SnBi_3$ and $Pt/SnBi_3$ films were coated with N719 dye by soaking the film for ca. 36 h in a $2.73 \times 10^{-4}$ mol/l ethanol to get $SnBi_3$, $Pd/SnBi_3$ and $Pt/SnBi_3$ electrodes with 17 mm thickness. The counter electrode consisted of the same conducting glass coated with graphite film was also made. The counter electrode was placed directly on the top of the dye coated $SnBi_3$, $Pd/SnBi_3$ and $Pt/SnBi_3$ film, leaving the two ends of the glass for application of electrical contact. The electrolyte containing 0.3 M KI and 0.03M $I_2$ in acetonitrile was soaked up by the capillary force into the inter electrode space. I–V characteristic for the cell was examined in the presence of light using an ELH-lamp at a light intensity of 100 mW/cm$^2$. The voltage was recorded using Keithly voltammeter 175A and the current using a Keithly electrometer 614. The fill factor was calculated using the following relation:[24] $FF = V_m I_m / V_{OC} I_{SC,}$ where $V_m$ and $I_m$ are respectively, voltage and current for maximum power output. The solar cell efficiency is calculated ($\eta_y$) using the following relation: [24] $\eta_y = V_{oc} I_{sc} FF / P_{in}$ where $P_{in}$ is the power of the incident light. Monochromatic incident photon conversion efficiency (IPCE) spectra were measured using a home-made lock-in-based setup equipped with a calibrated Si/Ge photodiode, as reference detector. The light from the halogen and Xenon lamps was spectrally dispersed using a monochromator with a set of gratings to cover the wavelength range from 300 to 900 nm. The obtained current densities were converted into incident photon-to-current conversion efficiencies (*IPCE*) by using equation: $IPCE= ((1240/\lambda) * (I/P_{in}))*100$ where $P_{in}$=30W

**2.5. Electrical properties**

The electrical properties of the prepared oxides were performed via compressing the powder of the sample under a pressure of 6 tons cm$^{-2}$ to form pellets. The two parallel

surfaces of the pellets (7 mm diameter and 1mm thickness) were coated with silver paste to ensure good electrical contact. Each pellet of the sample investigated was located in a sample holder inside an oven with a temperature controller of ± 0.1°C accuracy. All the samples were heated to 473 K for 1 hour before measuring to confirm the non-exiting of the hydrated water on the oxides surfaces. The electrical measurements were carried out at a constant voltage (1 volt) and in a frequency range from 300 Hz to 1 MHz and in temperature range from 25 to 500 °C by using programmable automatic LCR bridge (model RM6306 Philips Bridge).

## 3. Results and discussion

### 3.1. XRD and TEM investigation

The X-ray diffraction patterns of metal free $SnBi_3$ composite as well as Pd/Pt containing composites are shown in Fig. 1. In the Sn- and Bi-rich composite; formed at the nominal ratio 1:3, an appearance of the $Bi_2Sn_2O_7$ phase is noticed via existence of sharp and strong peaks at $2\theta$ =24.14◦ (220), 33.6◦ (444)and 59◦ (622). This pattern also shows peaks for tetragonal $SnO_2$ at $2\theta$ = 26.01◦ (110), 36.9◦ (200), 60.09◦ (310) and 68.2◦ (112) (comparable to the values of JCPDS 41-1445) together with peaks ascribed to the tetragonal β-$Bi_2O_3$ phase (PDF NO. 27-50) at $2\theta$ = 32.69◦ (220), 46.22◦ (222), 50.08◦ (440), 54.27◦ (203) and 55.48◦ (421). A residual peak at $2\theta$ = 41.5 (221) due to the α-$Bi_2O_3$ phase is also depicted. The XRD pattern of Pd/$SnBi_3$ indicates major peaks for the $Bi_2Sn_2O_7$ phase at $2\theta$ = 24.0◦ (220), 28.2◦ (222), 31.9◦ (220), 33.6◦ (444) and 53.1◦ together with peaks ascribed to the β-$Bi_2O_3$ phase at $2\theta$ = 27.4◦ (120), 31.76◦ (002), 46.22◦ (222), 54.27◦ (203), 55.27◦ (421), 57.75◦ (402). This pattern showed additional small intensity peaks at 2θ = 40◦ and 46◦ attributable to (111) and (200) planes of deposited Pd nanoparticles [25], as compared to the pattern of $SnBi_3$. These peaks are indexed to face-centred cubic Pd (Joint Committee on Powder Diffraction Standards (JCPDS) Card No. 05-0681, a = 3.889 A). It appeared that Pd incorporation stimulates the evolution of new peaks for $Bi_2Sn_2O_7$ (28.2◦ (222), 31.9◦ (220), and 53.1◦) and β-$Bi_2O_3$ (27.4◦ (120), 31.76◦ (002), 57.75◦ (402)) phases and declining those belong to the $SnO_2$ phase appeared in the diffraction of $SnBi_3$. Accordingly, the disappearance of the $SnO_2$ phase in favour of the $Bi_2Sn_2O_7$ growth signifies the dissolution of $SnO_2$ in $Bi_2O_3$. Furthermore, the α-$Bi_2O_3$ phase was completely faded supporting the exposure of the β- $Bi_2O_3$ phase. This highlights that the adopted procedure as well as Pd incorporation is succeeded in obtaining a more

stabilized phase of β-$Bi_2O_3$ although literatures [26] used to verify the stability of α-$Bi_2O_3$ at high temperatures. A significant decrease in the crystallite sizes of the Pd/$SnBi_3$ sample was observed relative to the $SnBi_3$ sample as the former suffers a significant decrease in crystallization intensities.

On the other hand, the Pt/$SnBi_3$ pattern; of comparative decreased intensity to the latter, shows nearly all the diffraction peaks that indexed to the tetragonal $SnO_2$ (2θ=26.4, 51.64) and tetragonal $Bi_2Sn_2O_7$ structure (JCPDS: 34-1203) with peaks localized at 2θ= 24.14◦, 29.06◦, 33.55◦, 51.6◦ and 54.78◦. Simultaneously, peaks correlated to β-$Bi_2O_3$ are also shown via exposing diffractions at 2θ= 32.46◦ and 46.68◦. Small bands at 2θ=40◦, 46◦ and 68◦ due to 111, 200 and 211 spacings, respectively attributable to Pt metal crystallites [27] are depicted. Pt incorporation did not affect $SnO_2$ phase; as has been seen for Pd, but indeed decreases its percentages compared to those present in the $SnBi_3$ sample. Accordingly, there is a slight increase in the lattice constants of the composites compared to pure $SnO_2$, which indicates that some of the $Pt^{4+}$ ions (with ionic radius 7.7 nm) incorporates into the $Sn^{4+}$ site of the $SnO_2$ (7.2 nm) lattice rather than with $Bi_2O_3$ (10.3 nm). The average crystallite sizes estimated from the prominent diffraction peaks of $SnO_2$ (2θ = 26.4°), $Bi_2Sn_2O_7$ (2θ=28.8°) and β-$Bi_2O_3$ (2θ=29.16°); in the latter sample, using Scherrer's equation were 12 nm, 14 and 7.8 nm, respectively. These values were the lowest compared to metal free and Pd containing $SnBi_3$ samples proposing that introduction of Pt nanoparticles into the crystalline matrix of $SnBi_3$ led to crystalline imperfection that by its turn causes a decrease in signals intensities.

The morphologies of synthesized samples were examined by TEM. The TEM image of $SnBi_3$ shows irregular polyhedral crystalline structure composed of tetragonal and hexagonal shapes with average sizes equal 72±2 nm (Fig. 2a). This image also shows an amorphous region with no agglomeration. The TEM image of Pd/$SnBi_3$ shown in Fig. 2b revealed a polyhedral-like structure consisted mainly of cubic and hexagonal shaped nanocrysallites with an average size equal 44± 2 nm. The HRTEM image of the nanoparticles (seen as an inset) exhibited resolved lattice fringes at 1.54 Å and 1.38 Å indexed to (220) and (400) planes of β-$Bi_2O_3$and $Bi_2Sn_2O_7$, respectively. This indicates the close proximity of crystallized β-$Bi_2O_3$ and $Bi_2Sn_2O_7$ phases. This close interconnection between the two phases is supposed to favor the photo-induced electrons transfer between the phases that assume to reduce the recombination of the

photo-induced electrons and holes and improve the photocatalytic activity of the catalysts. The inset of Fig. 2b also shows the SAED image of Pd/$SnBi_3$. The planes (220), (444) and (002) appeared in SAED image and correlated, respectively to $Bi_2Sn_2O_7$ and β-$Bi_2O_3$ are agreed with the results obtained from XRD analysis. This clear and bright SAED image is indeed confirmed the intimate contact between β-$Bi_2O_3$ and $Bi_2Sn_2O_7$ phases, depicted previously via HRTEM. Fig. 2c presents the TEM image of Pt/$SnBi_3$. It shows a wrinkled sheet like structure with average sizes equal 22 nm that encapsulated Pt nanoparticles of circular shape. The HRTEM-inset in this figure shows distances at 3.36 Åand 3.05 Å, which correspond to (110) and (220) planes of $SnO_2$ and $Bi_2Sn_2O_7$ phases, respectively. This signifies the close proximity of the two phases and the facile electron transfer between them. The average crystallites size of this sample was comparatively small; as committed previously via XRD analyses, explaining the role of the pluronic-123 template in slowing the nucleation rate via the sol–gel technique; compared with Pd/$SnBi_3$. Accordingly, Pt interacted in a different way with $SnBi_3$ and resulted in a homogeneous nucleation so as to producing such regular cubic and hexagonal structures and rather stimulates the existence of $SnO_2$ rather than $Bi_2O_3$ promoted by Pd presence.

**3.2. FTIR spectroscopy**

Figure 3 shows the FT-IR spectra of $SnBi_3$ and Pd(Pt)/$SnBi_3$ samples calcined at 500°C. The observed spectra showed similar prominent bands related to O-H stretching vibrations, OH deformation modes and $CH_2$ stretching modes at 3422 $cm^{-1}$, 1629-1636 $cm^{-1}$ and 2850 (2920) $cm^{-1}$, respectively. In concordance with the later bands (2850 and 2920 $cm^{-1}$), a mode at 1385 $cm^{-1}$ due to C-H stretching was existed in all samples characterizing the presence of residual amounts of the Pluronic template. Only in Pd/$SnBi_3$, a band at 1228 $cm^{-1}$ due to C-O stretching modes is observed reflecting to what extent the template is chemically grafted to the surface of this sample, as also estimated from increasing the intensity of the bands in the region from 1550 to 1050 $cm^{-1}$**.** However, this is not the case in Pt/$SnBi_3$. Accordingly, this signifies distinctive reaction approaches for Pt and Pd towards $SnBi_3$ nanocomposites and to the pluronic template. In this context, Pt/$SnBi_3$ indicates lower intense bands compared to rest of samples demonstrating that the extent of interaction of Bi-O and Sn-O bonds with Pt was much stronger than with Pd. This former strong interaction

affected severely the intensity as previously influenced the crystallinity; as traced by XRD of this sample. At lower wavenumbers, several bands characteristic of the oxygen-metals/stretching mode at 846, 625 and 533 $cm^{-1}$ (for all samples), together with another band at 920 $cm^{-1}$ (only shown for $Pd/SnBi_3$) are present.[28, 29] The former bands are assigned, respectively to vibrational absorption of the Bi–O–Bi bonds, the Sn-O stretching vibration and vibrations of Bi–O bonds in the distorted $BiO_6$ octahedral units. The broad band at 920 $cm^{-1}$ can be assigned to Bi(3)–O–Bi(6) specific vibrations and/or to vibrations of pyrochlore $Sn_2Bi_2O_7$units [25] since this specific sample; $Pd/SnBi_3$, indicates high percentages of pyrochlore compared to the rest of samples; as confirmed from XRD results. The broadness of the 920 $cm^{-1}$ band explains that $Sn_2Bi_2O_7$ in $Pd/SnBi_3$ was not completely pure probably due to its association with the crystalline β-$Bi_2O_3$ phase; as also revealed via XRD and TEM investigations. A regular shift of OH deformation modes to high frequencies from 1629 $cm^{-1}$; in $SnBi_3$, to 1631 $cm^{-1}$ ($Pd/SnBi_3$) and 1636 $cm^{-1}$ ($Pt/SnBi_3$) was observed. This can be explained by an increase in force constant when the atomic number increases.

### 3.3. Surface texturing properties

Fig. 4 displays the nitrogen adsorption–desorption isotherms of metal free $SnBi_3$ as well as Pt(Pd) supported on $SnBi_3$ nanostructures. The nitrogen sorption isotherms of all samples are similar and belong to the type IV with clear hysteresis loops, indicating the formation of mesoporous structures. However, shifting the loop to relatively higher pressure ($P/P_0$= 0.72-1) in case of $Pd/SnBi_3$, suggests an increase in the size of the mesopores, which may be resulted from the stacking of $SnO_2$ and $Bi_2O_3$ crystallites. Furthermore, the BET surface area of the $SnBi_3$ sample was calculated to be 25 $m^2/g$ exceeding those of Pt (19 $m^2/g$) and Pd (12 $m^2/g$) containing $SnBi_3$ composites. The marked decrease in the specific surface area following Pd(Pt) loading reflects the well dispersion of these metal nanoparticles deep inside the nanocomposite pores. It seems also that Pd (12 $m^2/g$) incorporation led to a more dispersion than Pt (19 $m^2/g$) as also confirmed from diminishing the pore volume and pore radius of the former sample compared to the latter (not shown). Moreover, the pore size distribution curves; plotted using BJH method, for $SnBi_3$ and $Pt/SnBi_3$ samples exhibited average pore diameters maximized at 2.5 and 10 nm whereas $Pd/SnBi_3$ indicated trimodal distributions maximized at 2, 2.5 and 20 nm. By

comparing the pore size distribution profiles of former samples relative to the later, indicate that Pd incorporation stimulates the existence of wide mesopores via evolution of the pore size at 20 nm. All the isotherms belong to category H3 type of pores, which do not exhibit limiting adsorption at high $P/P_0$, and arouse due to aggregation of plate-like particles giving rise to slit-shaped pores. This indicates that the assembly of $SnO_2$ and $Bi_2O_3$ heterostructures via using structure directing template pluronic-123 provoked mesoporous array, most probably reflected by the $Bi_2Sn_2O_7$ formation. This is ascertained in the $Pd/SnBi_3$ sample that indicates high mesoporosity percentages and in the same time evokes high percentages from $Bi_2Sn_2O_7$ structure.

**3.4. Optical study**

The optical absorption of metal free $SnBi_3$ as well as Pd/Pt containing $SnBi_3$ nanostructures were measured by UV-Vis diffuse reflection spectroscopy and the results are shown in Fig. 5. The absorbance edge of the as-prepared $SnBi_3$ sample is located at the wavelength of 550 nm whereas Pd/Pt containing composites are located in the wavelength range from 500 to 800 nm. The band gap energies of the as-prepared $SnBi_3$, $Pd/SnBi_3$ and $Pt/SnBi_3$ samples synthesized hydrothermally at 120$^o$C,via using pluronic-123, and determined from the plot of $(EA)^2$ vs. energy (E) (in-set Fig. 5) are found to be about 2.50, 2.30 and 2.34 eV, respectively. Such differences may be ascribed to the changes in crystalline phase and defects might be created following Pd/Pt incorporation. Decreasing the band gap value of $Pd/SnBi_3$ than rest of samples emphasizes that exposing β-$Bi_2O_3$ and $Bi_2Sn_2O_7$ besides the adopted hydrothermal method could have a positive impact on decreasing the band gap energy. The band gap value of $SnBi_3$ was lower than those reported in previous studies[30] correlated to pure $SnO_2$ and $Bi_2O_3$ phases. For $Pt/SnBi_3$ and $Pd/SnBi_3$ samples, the UV–Vis absorption was shifted into the visible region probably due to the well dispersion of Pt/Pd nanoparticles within the nanocomposites and to the introduction of isolated energy levels in the band gap of the composites semiconductors. This indeed indicates that the capabilities of these nanocomposites toward harvesting visible light are expected to increase as well as their photocatalytic performances. A significant increase in the absorption at wavelengths shorter than 450 nm for $SnBi_3$ exceeding those of Pd/Pt containing samples was noticed and assigned to the intrinsic band gap transition of $SnO_2$ and $Bi_2O_3$ nano-crystallites [6] as well as to the transition from the impurity level

in the semiconductors obtained via the strong adherence between them; rather than when metal incorporation takes place. The sample $Pt/SnBi_3$ has shown the lowest absorption and indicated a blue shift for the 300-350 nm band (305 nm) apart from the corresponding metal free mixed oxide ($SnBi_3$-335 nm) and $Pd/SnBi_3$ (320 nm) samples due to the decrease in crystallites size, as estimated from XRD and TEM results. On the other hand, no special surface Plasmon peak was noticed for Pd/Pt doped $SnBi_3$ (used to be at 390–450 nm) probably due to the well dispersion of Pd/Pt nanoparticles; of low amount, and to the presence of isolated energy levels in the band gap of the semiconductor [19] composite. Accordingly, the peak at 395 nm cannot be assigned to surface Plasmon resonance of Pd/Pt nanoparticles since it appeared in the Pd free $SnBi_3$ sample.

### 3. 5. Electrical properties

#### 3.5.1. Frequency and temperature dependency of a.c. conductivity

The AC electrical conductivity($\sigma_{AC}$) is a thermally activated process. Fig.S1 shows the temperature dependence of $\sigma_{AC}$ for $SnBi_3$, $Pd/SnBi_3$ and $Pt/SnBi_3$ nanocomposites. It was found that the a.c. conductivity increases with increase in temperature signifying the semiconductor behavior of the samples. As a consequence of structural changes, electrical conductivity could intensely be modified. The temperature dependence of $\sigma_{AC}$ also indicates that the electrical conduction in the material is governed by the Arrhenius relation:

$$\sigma_{AC} = \sigma_o \exp(E_a / k_B T) \qquad (1)$$

Where $\sigma_o$ is the pre-exponential factor, $E_a$ is the activation energies of the mobile charge carriers, $k_B$ is the Boltzmann's constant and T is the temperature in K. This relation shows two linear regions with different slopes indicative of the existence of two different conduction mechanisms in the measured temperature range. It was observed that the activation energies $E_{a1}$ and $E_{a2}$, which are corresponding respectively, to the temperature range 303-593 K and 593-773 K, performed at different frequencies indicate that $E_{a1}$ values were lower than those of $E_{a2}$. This difference may be due to the different conduction mechanisms and the instability of the $SnO_2/Bi_2O_3$ nanocomposites in the mentioned temperature range as established via DTA curves; in which an endothermic peak at ~ 300$^o$C for all samples was depicted. Oxygen vacancies and space charge polarization, generation of charge carriers and evolution of new phases may be responsible for the change in activation energy as a

function of temperature.[31] Oxygen vacancies may be created with an increase in the temperature. The $Bi_2O_3$ may form a solid solution with $SnO_2$ according to the following equation that has been rather confirmed via XRD results:

$$Bi_2O_3 \xrightarrow{SnO_2} V_{\ddot{O}} + 2O_0^x + 1/2O_2(g) \quad (2)$$

As indicated in Equation 2, the formation of solid solution in the $SnO_2$ lattice should increase the oxygen vacancy concentration .[32] In addition, $Bi_2O_3$ should contribute to the increase of negative charges due to the creation of the atomic defect $Bi^{\bullet}Sn$ at the interface, inducing the formation of positive oxygen vacancies.[33] Accordingly, bismuth oxide is responsible for the increase in defect concentration at the heterosturcture grain boundaries improving the electrical properties. Accordingly, $Pd/SnBi_3$ indicates very high conductivity compared to $Pt/SnBi_3$ (Fig. 6) whereas $SnBi_3$ reflects very low conductivity. This conceivably due to the inclusion of Pd metal within the nanocomposites $SnBi_3$ has established structural changes via exposing $Bi_2Sn_2O_7$ and β-$Bi_2O_3$ phases with the absence of $SnO_2$ phase; known as an insulator. Whereas Pt metal comprehends the the appreciable presence of the latter phase, as confirmed from XRD results. In addition, lowering the bang gap energy of Pd doped sample (2.3 eV) as well as its well dispersion in $SnBi_3$ ($S_{BET}$ =12 $m^2/g$) influences the conductivity. Introduction of additives which increase the concentration of cation vacancies can accelerate diffusion and facilitate the polymorphic transition. In this case, at high temperatures, the activation energy (relaxation energy) is large enough to create vacancies that are summing up energy required for vacancy creation and motion of charge carriers into vacancies.[31, 32] On the other hand, Fig. S1 shows also that a.c. conductivity increases with increasing frequency according to the expression:[33,34]

$$\sigma_{ac} = A\,\omega^s \quad (3)$$

Where $\sigma_{ac}$ is a.c. conductivity, A is constant independent of frequency, s is frequency exponent, ω is angular frequency. It was found that the value of s lie in the range $0 < s < 1$ and this type of behavior represents variable type of hopping conduction, which is in concordance with Elliot et al.[35] within certain temperature and frequency regimes.[36]

### 3.5.2. Frequency and temperature dependency of dielectric constant

The dielectric constant or relative permittivity ε` is calculated via using the following simplified form:

$\varepsilon` = (C/\varepsilon_0)(d/A)$ (4)

Where C is the capacitance, d is the thickness of pellets, $\varepsilon_0$ is the permittivity of free space ($8.854\times10^{-12}$ F/m) and A is the pellet area. The temperature dependence of dielectric constant ε` of the samples is shown in Fig. S2. It can be seen that the dielectric constant increases with temperature and decreases with frequency. This indicates a major contribution of ionic conductivity to the dielectric constant. The dielectric polarization mechanisms that contribute to the enhanced behavior of nanomaterials are space charge polarization (SCP) process.[37] SCP process plays an important part in our sample. Generally, nanostructured materials have about $10^{19}$ interfaces/$cm^3$, which is much higher compared to that of bulk solids.[38] The value of dielectric constant εr of $SnO_2$ nanoparticles is very high as compared to that of bulk $SnO_2$, reported at room temperature.[39] The interfaces with a large volume fraction in the nanostructured compacted samples contain a large amount of defects, such as microporosities, dangling bonds and vacancy clusters. These defects can cause a change of positive and negative space charge distributions in interfaces.[39-40] Negative and positive spaces in interfaces move towards positive and negative poles of the electric field, respectively. As they are trapped by defects, newer dipole moments will exist and SCP process will indeed takes place in the sample. Because the volume fraction of the interfaces of nano-size sample is larger than that of bulk materials, SCP is stronger than that in the bulk materials. Thus, $\varepsilon_r$ of $SnBi_3$, $Pd/SnBi_3$ and $Pt/SnBi_3$ nanoparticles is higher than those of the corresponding bulk. It was found that the dielectric constant of synthesized samples was in the following order $SnBi_3$< $Pt/SnBi_3$< $Pd/SnBi_3$ maximizing the influence of defect sites and polarization in the doped $SnBi_3$ samples.

**3.5.3.Temperature and frequency dependency of impedance**

Impedance is a far more general concept compared to resistance because it takes phase difference into consideration. In a.c.the resistance R is replaced by the Z which is sum of resistance and reactance. Impedance is given by, $Z= Z` + Z``$ (5)

Where, Z` is the real part and is expressed as $Re(Z)= Z`=|Z|\cos\theta$ and Z`` is the imaginary part of Z expressed as $Im(Z)=Z``=|Z|\sin\theta$, where θ being the phase angle. The plot of these graphs in complex plane is known as Cole–Cole plot for $SnBi_3$,

$Pd/SnBi_3$ and $Pt/SnBi_3$ samples (Fig.7). The impedance spectra exhibits ingle semicircular arcs with their centers lying below the real axis at a particular angle of depression. These plots suggest an electrical equivalent circuit composed of a resistance R and a capacitance C connected in parallel.[41] It is observed that the size of the plots decrease in the order: $SnBi_3$< $Pt/SnBi_3$ <$Pd/SnBi_3$, which attributed to the decrease in the value of the bulk resistance (R) in the same order. This indicates increasing the charge transfer of $Pd/SnBi_3$ compared to the other samples. The impedance spectra of $Pd/SnBi_3$ show a smaller circular radii compared to other samples revolving the role of the grain boundary contribution substantiated from the adherence of $\beta$-$Bi_2O_3$/$Bi_2Sn_2O_7$ phases; confirmed from XRD and TEM-EDX results.

**3.6. Photocatalytic performance of synthesized nanocomposites**

Methylene blue (MB) was adopted as a representative organic pollutant to evaluate the photocatalytic performance of the as-synthesized samples. The photocatalytic activities of the as-synthesized samples are shown in Fig. 8. The degradation efficiency is defined as $C/C_0$, where $C_0$ and C are the initial and reaction concentration of MB, respectively. As seen in Fig. 8, the order of the photocatalytic activity of the as-synthesized samples was $Pd/SnBi_3$>$Pt/SnBi_3$>$SnBi_3$. It is obvious that the photocatalytic activity of the $Pd/SnBi_3$ photocatalyst is significantly higher than those of metal free $SnBi_3$ and $Pt/SnBi_3$ nanocomposites either under UV or Visible light irradiations. The removal efficiency of $SnBi_3$ in the dark exhibits the maximum absorption that compromised of 25% in 60 min. This remarkable absorption indeed improved the photodegradation rate to reach 70% under UV irradiation and 43% under visible illumination for 150 min reaction time. On the other hand, $Pt/SnBi_3$ and $Pd/SnBi_3$ indicated MB dark adsorption comprised of 30%. Although they indicate similar dark adsorption, they presented unlike activity under UV light illumination (77% for Pt/SnBi3 vs. 98% for Pd/SnBi3) whereas under visible irradiation $Pt/SnBi_3$ exhibited removal efficiency comprised of 50% compared to 78% for $Pd/SnBi_3$. This comprehends that $Pd/SnBi_3$ is more active than $Pt/SnBi_3$ under both UV and Vis light irradiations and indeed exceeded those related to $SnBi_3$. These differences in the catalytic activity are dependent on spatial variations in the charge transfer at the $Pd/SnBi_3$ and $Pt/SnBi_3$ interfaces. To figure out if the photocatalytic activity is related to the dynamics of the separation and recombination of photoinduced electrons and holes, the photoluminescence (PL) study is carried out

and illustrated in Fig. 9. It can be seen that at the excitation wavelength of 380 nm, nanocomposite samples displayed a strong and broad emission peaks at ~ 460 nm. The emission intensity is significantly decreased in the $Pd/SnBi_3$ sample comparatively. This possibly indicates that the latter sample acted as traps for the photo-induced charge carriers. On the other hand, $SnBi_3$ can indeed absorb light to excite the valence band electrons to produce electron–hole pairs, however, it recombines rapidly followed by the $Pt/SnBi_3$ sample. Accordingly, the heterostructure consisting of $\beta$-$Bi_2O_3/Bi_2Sn_2O_7$ derived from $Pd/SnBi_3$ is considerably active if compared with that of $SnO_2/Bi_2Sn_2O_7$ in $Pt/SnBi_3$. Besides, the adsorption performance of the nanocomposites, the active species in the reaction process is another key factor that influences the photocatalytic reaction. To figure out the reactive intermediates exposed following irradiation of $Pd/SnBi_3$ and their role in the photodegradation reaction, the scavengers BQ (a quencher of $\bullet O_2^-$), TEOA (a quencher of $h^+$) and 2-propanol (IP) (a quencher of •OH) were employed. As was shown in Fig.10, the rate of MB degradation at low concentration of 2-propanol, indicates great inhibition revolving that the hydroxyl radicals are the major active species during the photocatalytic oxidation reaction. Further trapping experiments for detecting other actives pecies were again conducted during the photocatalytic degradation of MB in the presence of $Pd/SnBi_3$ under visible light irradiation. As observed, the degradation efficiency of MB was highly affected by the addition of 1 mM BQ (a quencher of $\bullet O_2^-$), but apparently not decreased with the addition 1 mM TEOA (a quencher of $h^+$). Therefore, the results show that •OH and $\bullet O_2^-$ are the two main active species play key roles in the degradation of MB rather than $h^+$. To further confirm the evolution of $\bullet O_2^-$ as reactive species, bubbling $N_2$ gas (30 ml/min) in the reaction medium while irradiating $Pd/SnBi_3$ by visible light indicates a marked decrease in the activity to be comprised of 40%. Thus, under visible illumination, the heterostructure $Pd/SnBi_3$ is excited to produce electron-hole pairs in both $\beta$-$Bi_2O_3$ (2.3 eV) and $Bi_2Sn_2O_7$ (2.7 eV)[42] since the energy of the visible light photon (2.9 eV) is greater than later oxides (scheme 1). Accordingly, electrons in the valence band of $\beta$-$Bi_2O_3$can be excited in an easier way compared to $Bi_2Sn_2O_7$ to produce electrons and holes. Reversely, the holes from the $V_B$ of $Bi_2Sn_2O_7$ were injected into that of $\beta$-$Bi_2O_3$. This creates an internal electrostatic potential in the space charge region that is beneficial to the separation of the photogenerated charge carriers. The electrons then

react with $O_2$ molecules to form $\bullet O_2^-$ to degrade MB in water together with the provoked •OH. Indeed, $Bi_2Sn_2O_7$ also share in enhancing the photocatalytic activity not only due to the formed heterojunction with β-$Bi_2O_3$ but also due to it's accepting migrated electrons from β-$Bi_2O_3$ and thus delaying the expected fast recombination between holes and electrons. On the other hand, since doping by Pd increases the optical response across the entire visible spectrum; as seen in diffuse reflectance results, reflecting that Pd might take its way between the interlayers between β-$Bi_2O_3$ and $Bi_2Sn_2O_7$ or on their surfaces due to varied ionic radii of Pd (0.86Å) and β-$Bi_2O_3$(1.03 Å) unlike the case between Pt and $SnO_2$. Pd metal is acknowledged to be used in electron reservoir or electron-transfer systems to optimize and/or improve the spatial charge carrier separation and transfer across the interfacial domain between $Bi_2Sn_2O_7$ and β-$Bi_2O_3$ upon visible light irradiation. The possible electron transfer processes that can occur in the Pd/β-$Bi_2O_3$-$Bi_2Sn_2O_7$ system during photocatalytic degradation of MB are transfer of electrons from (1) sensitized dye to the conduction band of β-$Bi_2O_3$, (2) sensitized dye to Pd particles, (3) from the CB of β-$Bi_2O_3$ to Pd, (4) from the CB of β-$Bi_2O_3$ to its VB (recombination) and sensitized dye to the shallow trap levels in the band gap of β-$Bi_2O_3$. Both processes (1) and (2) are possible in the case of Pd because of the position of its energy level. This electron transfer will continue until the overall Fermi level of the metal-modified β-$Bi_2O_3$ system shifts toward more negative potential. Once this level is reached, Pd discharges the stored electrons in to the solution where they react with dissolved oxygen to form $\bullet O_2^-$ and •OH radicals in turn. These active oxygen species react with the dye molecules and degrade them. On the other hand, the close proximity between $SnO_2$ and $Bi_2Sn_2O_7$ phases; in Pt/$SnBi_3$, and the delay in the facile electron transfer between them as compared to β-$Bi_2O_3$/$Bi_2Sn_2O_7$ phases; in Pd/$SnBi_3$, based on the consideration that Pt nanoparticles can form local Schottky junctions,[27] is probably due to the back donation expected from Pt (6.1 eV) metal of high work function; compared to pd (5.4 eV) ones. Accordingly, Pd can serve as electron reservoirs to accept the photogenerated electrons from the conduction band ($C_B$) of $Bi_2Sn_2O_7$.

It seems also that the mesoporosity character of Pd/$SnBi_3$ plays an important role in enhancing the catalytic properties that has also been substantiated via existence of the trimodal pores (2, 2.5, 20 nm) compared to other samples. This proposes that the reaction can takes place inside the pores as well as on the catalyst surfaces. In addition

the existence of C-O band; in FTIR results, never seen in other samples could also facilitate the formation of $\bullet O_2^-$ upon irradiation. On the other hand, exhibiting a comparative decrease photocatalytic performance of $SnBi_3$ under ultraviolet and visible light irradiations conveys the less importance of the $\alpha$-$Bi_2O_3$ phase and indeed the presence of substantial amounts of $SnO_2$ together with $\beta$-$Bi_2O_3$ and $Bi_2Sn_2O_7$ phases those constitute the most active sites. The decreased crystallinity of the $Pt/SnBi_3$ sample; as devoted from XRD and IR data, could also affect the electron transfer in a facile way comparatively. Specifically, these defects are considered as important factors influencing the photocatalysis process since it could act as an electron-hole recombination center, resulting in a low photocatalytic activity. The aforementioned enhanced photocatalytic and electrical conductivity capabilities of our synthesized mesoporous nanocomposities; and most importantly Pd/$\beta$-$Bi_2O_3$/$Bi_2Sn_2O_7$, indicates that these materials could be advantageous for application in DSSCs .

### 3.7. Photovoltaic properties

Fig. 11 shows the current density-voltage characteristics of the DSSCs with different nanocomposite counter electrodes under visible light illumination (100 $mWcm^{-2}$). The derived photovoltaic parameters, such as open-circuit voltage ($V_{oc}$), short-circuit currentdensity ($J_{sc}$), fill factor (FF) and conversion efficiency ($\eta_y\%$) are summarized in Table 1. The DSSC with $Pt/SnBi_3$ working electrode perform poorly, the photovoltaic parameters being $J_{sc}$ 0.063 $mAcm^{-2}$; typical to that of $SnBi_3$, $V_{oc}$ 230 mV, FF 0.33 and $\eta_y$ 0.04%. The poor photovoltaic performance of the DSSC with $Pt/SnBi_3$ compared to $Pd/SnBi_3$ (of exceeding conversion efficiency reaching 0.2%) electrode can be attributed to the high over voltage losses on the electrode of the former photocatalyst due to its insufficient electrocatalytic activity for $I_3^-$ reduction. Accordingly, increasing the FF value of the later photocatalyst indicates that the heterojunction Pd/$\beta$-$Bi_2O_3$-$Bi_2Sn_2O_7$ was the one responsible for improving the Jsc performance. The Pd/$\beta$-$Bi_2O_3$-$Bi_2Sn_2O_7$ hetero-junction film exhibited an almost 1.7-fold higher photocurrent density (0.108 $mA/cm^2$) than Pt containing nanocomposite (0.063 $mA/cm^2$) and metal free $SnBi_3$ (0.062 $mA/cm^2$) film under illumination. This enhanced Photoelectrochemical performance is probably due to the increased optical absorption and efficient photogenerated carrier's separation at the Pd/$\beta$-$Bi_2O_3$-$Bi_2Sn_2O_7$ interface. Additionally, the $\beta$-$Bi_2O_3$ film has a more negative onset potential

compared to $Bi_2Sn_2O_7$ film (see scheme 1). Accordingly, dye absorbs photons (light) and become photoexcited that by its turn inject electrons into the conduction band of β-$Bi_2O_3$ (donor-acceptor interface) i.e. the photo-excited state is formed at the interface where the charge separation takes place, for sake of increasing photodynamic efficiency (light-to-electricity conversion). Figure S3 shows IPCE% as a function of wavelenghth for the three cells. It has been acknowledged that IPCE was dominated by light-harvesting efficiency, quantum yield of electron injection and the efficiency of collecting the injected electrons.[43] Compared to Pt/$SnBi_3$ cell, the IPCE of Pd/$SnBi_3$ and $SnBi_3$ give values equal 58% and 43% at 580 nm and 605 nm, respectively whereas the former indicates IPCE% of 27 at 580 nm. The films of both Pd/$SnBi_3$ and $SnBi_3$ had a higher IPCE in wavelength range from 500 nm to 850 nm than Pt/$SnBi_3$. This was in harmony with photovoltaic values and specifically those of conversion efficiency present in Table 1. However this not the case to the data in Fig. 5 in which the sequence in the visible light absorption was dominated by Pt(Pd) followed by the mother sample. This indicates that the weak photovoltaic energy conversion of Pt/$SnBi_3$ could be due to the presence of defects at the disordered surface, enhancing the recombination of photogenerated charge carriers. This is emphasized earlier via increasing defects; at which an electron-hole recombination process occurred, on Pt/SnBi3 due to decreasing its crystalinity comparatively. Interestingly, the working electrode assembled of Pd/β-$Bi_2O_3$-$Bi_2Sn_2O_7$ displayed an improved photo-current response over those prepared with GO/α-$Bi_2O_3$ and Ag/GO/α-$Bi_2O$.[44]

**3.8. Picosecond resolved spectra**

Both the absorption and photoluminescence (PL) spectra of Pd/$SnBi_3$ capped by citrate ions are shown in Figure 12. The absorption maximum is noticed at 330 nm (Fig.12a). As can be observed in Figure 12b, upon 300 and 375 nm laser excitation, strong emissions at 420 and 480 nm (Fig. 12c) were, respectively developed. A significant overlap between the excitation (usually similar to optical absorption curve of pure compound) of Pd/$SnBi_3$ and their emission bands was obtained, which is one of the key criteria for Förster resonance energy transfer (FRET) dynamics. Indeed, we propose FRET between donor-acceptor pair transition of Pd/$SnBi_3$ nanocomposites in which the mechanism involves a donor excited electronic state, which may transfer its excitation energy to a nearby acceptor in a nonradiative fashion through long-range dipole−dipole interaction.[45] More specifically, the hetero-junction between β-$Bi_2O_3$

and $Bi_2Sn_2O_7$ are the key for charge transfer in the nanocomposite, as emphasized in scheme 1and supported by TEM-EDX and PL data. The appearance of different states of free exciton reflects the good optical property of the $Pd/SnBi_3$ nanoarchitecture. In principle, if the fluorescence emission spectrum of the donor molecule overlaps the absorption spectrum of an acceptor molecule, and if the two are within a minimal distance from one another (1−10 nm), the donor can directly transfer its excitation energy to the acceptor via exchange of a virtual photon.[46] The donor thus decays to the ground state while the acceptor is still excited. A significant decrease in $Pd/SnBi_3$ lifetime was observed in the following sequence: 420 > 460≈ 500 nm, as shown in Fig.13a,b. In particular, the fast component which contributes nearly 90% of decay shows a major increase in lifetime from 0.04 to 0.118 ns (at 460 nm) and 0.138 ns (at 500 nm) in the $Pd/SnBi_3$ nanocomposite. This indicates that a major population of the charge injection process occurs with a greater rate constant as high as $10^9$ $S^{-1}$ if we compare only the fast component of the emission transients. 90% of the emission decay of $Pd/SnBi_3$ nanocomposites occurs with a lifetime of 0.04 ns indicating that the major fraction of the charge injection event occurs on an ultrafast time scale. A significant decrease in $Pd/SnBi_3$ fluorescence lifetime ($\tau_{av}$) is observed in the sequence 420 >500 ≥ 460 nm and these fluorescence lifetime are summarized in Table 2. On the other hand, the decreased efficiency of $Pt/SnO_2$-$Bi_2Sn_2O_7$ hetero-junction was due to the slower component of 0.04 ns that generates contribution comprised of 60% whereas the decay in $SnBi_3$ composite indicates contribution equal 40%. This means that decreasing the percentages carriers at the ultrafast time scale affects seriously the activity of photo-responsive reactions of Pd/ β-$Bi_2O_3$-$Bi_2Sn_2O_7$ and $Pt/SnO_2$-$Bi_2Sn_2O_7$ samples. The photoluminescence lifetime of Pd/β-$Bi_2O_3$-$Bi_2Sn_2O_7$ and $Pt/SnO_2$-$Bi_2Sn_2O_7$ was on the order of nanoseconds, and the photoluminescence lifetime of the former is exceeding that of the later. A longer PL lifetime means lower recombination rate of the electron–hole pairs, and thus higher photocatalytic activity is notifed for the former comparatively.

**4. Conclusion**

The synthesized composite consisting of β-$Bi_2O_3$ and $Bi_2Sn_2O_7$ stimulated by Pd has explored high electrical and photocatalytic functionalities. The enhanced photocatalysis of Pd/β-$Bi_2O_3$-$Bi_2Sn_2O_7$ during MB degradation under visible light irradiation (9.2 x$10^{-3}$$min^{-1}$); which was 4 fold the value of $Pt/SnO_2$-$Bi_2Sn_2O_7$ (3.0 x$10^{-}$

$^{3}min^{-1}$), was due to the facile charge transfer on an ultrafast time scale; as devoted from picosecond data, facilitated by the hetero-junction exhibited between β-$Bi_2O_3$/$Bi_2Sn_2O_7$ phases and to the enhanced mesoporosity. The enhanced photocatalytic activity of the later photocatalyst was also assisted by the evolution of $O_2$.- and ·OH radicals emphasizing the role of photogenerated electrons rather than holes in the photo-oxidation reaction. In order to explore the multifunctionality of this unique bismuth-containing system, this material is explored as the counter electrode of DSSCs and exhibited improved electrocatalytic activity for $I^-/I_3^-$ redox reaction and enhanced electrolyte diffusion capacity. This sample (Pd/β-$Bi_2O_3$/$Bi_2Sn_2O_7$) accordingly indicated very high electrical conductivity compared with Pt/$SnO_2$/$Bi_2Sn_2O_7$ whereas $SnBi_3$ reflects no conductivity.This conceivably attributed to the inclusion of Pd metal within the nanocomposites and its influence in establishing structural changes via exposing $Bi_2Sn_2O_7$/β-$Bi_2O_3$ hetero-junction with the absence of $SnO_2$ phase ;known as an insulator.

**References**

1. W.D. He, W. Qin, X.H. Wu, X.B. Ding, L. Chen, Z.H. Jiang, Thin Solid Films, 2007, 515, 5362.
2. S. J. A. Moniz, D. Bhachu, C. S. Blackman, A. J. Cross, S. Elouali, D. Pugh, R.Q. Cabrera, S. Vallejos, Inorg. Chim. Acta, 2012, 380, 328.
3. J.-y.Xia, M.-t.Tang, C. Cui, S.-m. Jin, Y.-m. Chen, Trans. Nonferrous Met. Soc. China, 2012, 22, 2289.
4. T.-C. Kuo, Y.-L. Kuo, W.-C. J. Wei, J. Eur.Ceram.Soc. 2011, 31, 3153.
5. M. M. Mohamed, M. S. Al-Sharif, Appl. Catal. B: Envir. 2013,142– 143, 432.
6. A. Hameed, T. Montini, V. Gombac, P. Fornasiero J. Am. Chem. Soc. 2008,130, 9658.
7. J. Eberl, H. Kisch, Photochem. Photobiol. Sci. 2008, 7, 1400.
8. Y. Wang, Y.Y. Wen, H.M. Ding, Y.K. Shan, J. Mater. Sci. 2010, 45, 1385.
9. P. Shuk, H.D. Wiemhofer, U. Guth, W. Gopel, M. Greenblatt, Solid State Ionics, 1996, 89, 179.
10. L. Moens, P. Ruiz, B. Delmon, M. Devillers, Appl. Catal. A, 1998, 171, 131.
11. L. Moens, P. Ruiz, B. Delmon, M. Devillers, Appl. Catal. A, 1999, 180, 299.
12. J. Sabate, J. M. Bayona, A. M. Solanas, Chemosphere, 2001, 44, 119.
13. D. B. Kittelson, J. Aerosol Sci. 1998, 29, 575.

14. H.T. Yu, J Environ Sci. Health Part C: Environ Carcinog & Ecotoxicol Rev. 2002, 20, 149; Y. C. Lin, W. J. Lee, H. C. Hou, Atmos. Environ. 2006, 40, 3930.
15. S. M. Correa, G. Arbilla, Atmos. Environ. 2006, 40, 6821.
16. D. Dunn, G. Hostetler, M. Iqbal, V. R. Marcy, Y. G. Lin, B. Jones, L. D. Aimone, J. Gruner,; M. A. Ator, E. R. Bacon, S. Chatterjee, Bioorg. & Medic. Chem. Lett. 2012, 22 (11), 3751.
17. D. Kibanova, J. Cervini-Silva, H. Destaillats, Environ. Sci. Technol. 2009, 43, 1500.
18. H. Tsuchiya, J.M. Macak, L. Taveira, E. Balaur, A. Ghicov, K. Sirotna, P. Schmuki, Electrochem. Commun. 2005, 7, 576.
19. M. M. Mohamed, S. A. Ahmed, Microp. Mesop. Mater. 2015, 204, 62.
20. W.D. He, W. Qin, X.H. Wu, X.B. Ding, L. Chen, Z.H. Jiang, Thin Solid Films, 2007, 515, 5362.
21. S.J.A. Moniz, C.S. Blackman, C.J. Carmalt, G. Hyett, , J. Mater. Chem. 2010, 20, 7881.
22. Q. Tian, J. Zhuang, J. Wang, L. Xie, P. Liu, Appl. Catal. A, 2012, 425–426, 74.
23. F. N. Sayed, V. Grover, B. P. Mandal, A. K. Tyagi, J. Phys. Chem. C, 2013, 117, 10929.
24. Z. S. Wang, F. Y. LI, C. H. Huang, L. Wang, M. Wei, L. P. Jin and N. Qiang, J. Phys. Chem. B, 2000, 104, 9676.
25. L. Bourja, B. Bakiz, A. Benlhachemi, M. Ezahri, J.C. Valmalette, S. Villain, J.R. Gavarri, J. Taibah Univ. Sci. 2010, 4, 1.
26. R. Nie, J. Shi, W. Du, Z. Hou, Appl. Catal. A, 2014, 473, 1.
27. M. M. Ibrahim, S. A. Ahmed, K. S. Khairou, M. M. Mohamed, Appl.Catal. A, 2014, 475, 90.
28. A.N. Desikan, L. Huang, S.T. Oyama, J. Phys. Chem. 1991, 95, 10050.
29. K.V.R. Chary, V. Vijayakuma, P.K. Rao, Langmuir, 1990, 6, 1549.
30. F. Pourfayaz, A. Khodadadi, Y. Mortazavi, S.S. Mohajerzadeh, Sens. Actuators B, 2005,108, 72.
31. S. K. Barik, R. N. P Choudhary, P. K. Mahapatra, J. Alloys Compds. 2008, 459, 35.
32. S. K. Patri, R. N. P Choudhary, B. K. Samantary, J. Alloys Compds. 2008, 459, 333.

33. H. Frohlick, Theory of Dielectrics, Oxford University press, 1956.
34. S. R. Elliott, Ibid. 1977, 36, 1291.
35. S.R. Elliott, Philosophical Magazine, 1978, 37, 135.
36. S.Z.A. Zaidi, J. Beynon, C.B. Steele, J. Mater. Sci. 1997, 32, 3921.
37. N. Kumari , A. Ghosh, S.Tewari , A. Bhattacharjee , Mater. Sci. Semicond. Proc. 2013, 16, 905.
38. W.Y. Wang, Y.P. Xu, D.F. Zhang, X.L. Chen., Mater. Res. Bull. 2001, 36, 2155.
39. H. Frohlick, Theory of Dielectrics, Oxford University press, 1956.
40. M. Ghosh, C.N.R. Rao, Chem.Phys. Lett. 2004, 393, 493.
41. A. Chandra Bose, P. Balaya, P. Thangadurai, S. Ramasamy, J.Phys. Chem. Solids, 2003, 64, 659.
42. Y. Xing, W. Que, X Liu, H. M. A. Javed, Z. He, Y. He, T. Zhou, RSC Adv. 2014, 4, 49900.
43. N. G. Park, J. van de Lagemaat, A. J. Frank, J. Phys. Chem. B 2000, 104, 8989.
44. T. Som, G. V. Troppenz, R. R. Wendt,M. Wollgarten, J. Rappich, F. Emmerling, K. Rademann, Chem. Sus. Chem. 2014, 7, 854.
45. C. M. Drain, A. Varotto, I. Radivojevic, Chem. Rev. 2009, 109, 1630.
46. D. Liu, W. Wu, Y. Qiu, S. Yang, S. Xiao, Q. Q. Wang, L. Ding, J. Wang, Langmuir, 2008, 24, 5052.

**Figures Captions**

Fig. 1: XRD patterns of: a) $SnBi_3$ b) $Pd/SnBi_3$ c) $Pt/SnBi_3$

Fig. 2: (a) TEM image of $SnBi_3$, (b) TEM image of $Pd/SnBi_3$ and the inset figure is the magnification of the shaded red area together with elaborating Pd nanoparticles and SAED image (c) TEM image of $Pt/SnBi_3$ and inset figure is the magnification of the area under the red arrow where white arrows point to Pt nanoparticles

Fig. 3: FTIR spectra of: a) $SnBi_3$ b) $Pd/SnBi_3$ c) $Pt/SnBi_3$

Fig. 4: Adsorption-desorption isotherm and the corresponding pore size distribution curves of (a) $SnBi_3$ (b) $Pd/SnBi_3$ c) $Pt/SnBi_3$

Fig. 5: UV–Vis absorption spectra of $SnBi_3$, $Pd/SnBi_3$ and $Pd/SnBi_3$ and the inset is the corresponding Energy gap ($E_g$) curves.

Fig. 6: The comparison of Ac-conductivity values of: a) $SnBi_3$ b) $Pd/SnBi_3$ c) $Pt/SnBi_3$

Fig. 7: Z``-Z` plot of: a) $Pd/SnBi_3$ b) $Pt/SnBi_3$ c) $SnBi_3$

Fig. 8: Photocatalytic degradation of MB dye at 298 K under UV and Visible light (in-set) illumination in presence of $SnBi_3$, $Pd/SnBi_3$ and $Pt/SnBi_3$: Reaction conditions: 100 mg catalyst, 20 ppm dye conc., V = 0.1 L, UV lamp intensity = 60 $mWcm^{-2}$ and vis lamp intensity = 120 mW $cm^{-2}$.

Fig. 9: Photoluminescence spectra of $SnBi_3$, $Pd/SnBi_3$ and $Pt/SnBi_3$

Fig. 10: Effect of reactive intermediates (isopropanol, IP; p-benzoquinone, BQ; triethanolamine, TEOA) on the activity of $Pd/SnBi_3$ towards MB photooxidation (reaction conditions: 100 mg catalyst, 20 ppm dye conc., V = 0.1 L, Vis lamp intensity = 120 mW $cm^{-2}$).

Fig. 11: Current–voltage characteristic curves for photo-electrochemical cell based on N719 dye-sensitized of: a) $SnBi_3$, b) $Pd/SnBi_3$ and c) $Pt/SnBi_3$

Fig. 12: UV-vis absorption spectra of $Pd/SnBi_3$ (pink), in citrate solution,(a); and room-temperature PL spectra at two different excitation wavelength at 300 (blue) and 375 (Red) nm), (b); and PL spectra showing emmission spectra at 420 (blue) and 480 (red) nm,(c).

Fig. 13: The picosecond-resolved fluorescence transients of $Pd/SnBi_3$ in citrate solution evolving emission wavelengths at 420, 460, and 500 nm upon excitation with laser source of 375 nm wavelengths, (a); and polarization gated picosecond resolved fluorescence spectra (b).

Scheme 1: Plot for electron–hole separation and transport at Visible-light driven $Pd/SnBi_3$ photocatalyst interface.

Table 1: Optical data of studied samples solar cell performances at illumination intensity of 100 mW/cm$^2$.

| Samples | $V_{OC}$ (mV) | $I_{SC}$ (mA) | FF | Efficiency ($\eta_y$)(%) |
|---|---|---|---|---|
| SnBi3 | 760 | 0.062 | 0.35 | 0.1 |
| Pd/SnBi3 | 464 | 0.108 | 0.52 | 0.2 |
| Pt/SnBi3 | 230 | 0.063 | 0.33 | 0.04 |

Table 2: Characterization of decay emissions of $Pd/SnBi_3$

| Detection wavelength | $\tau_1$(ns) | $\tau_2$(ns) | $\tau_3$(ns) |
|---|---|---|---|
| 420 | 0.04(90%) | 1.23(7%) | 6.62(3%) |
| 460 | 0.118(70%) | 1.334(23%) | 6.123(7%) |
| 500 | 0.138(24%) | 1.308(24%) | 6.185(6%) |

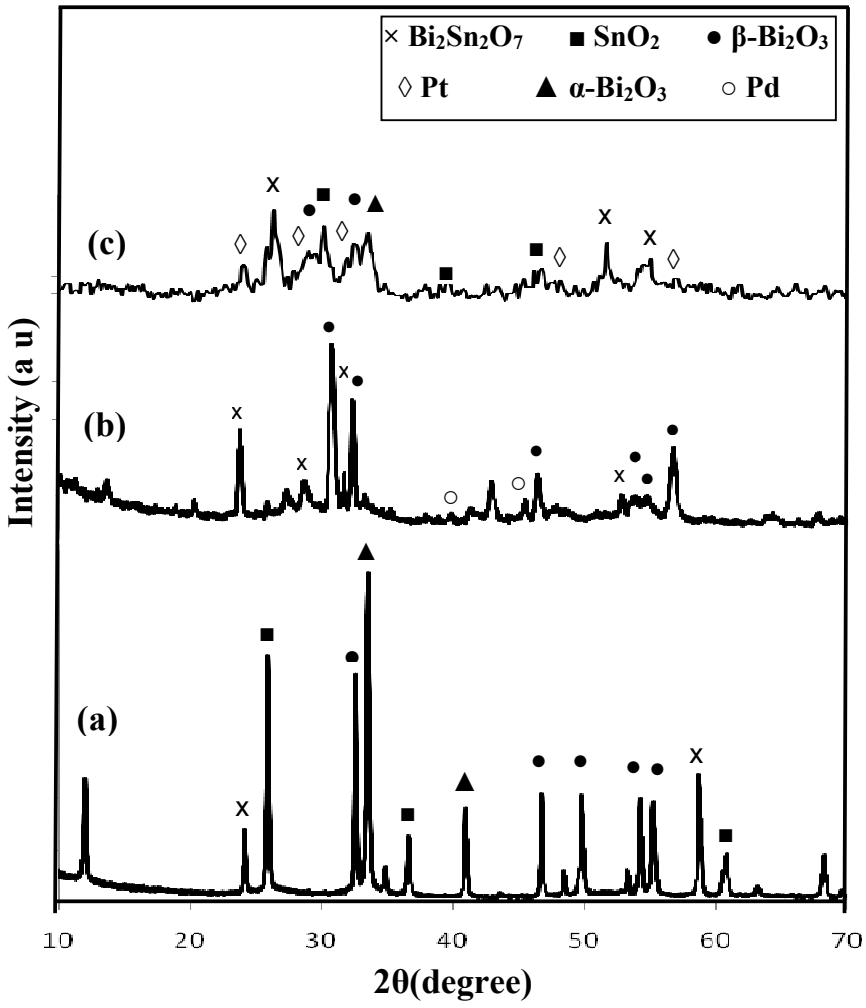


**Fig. 1**

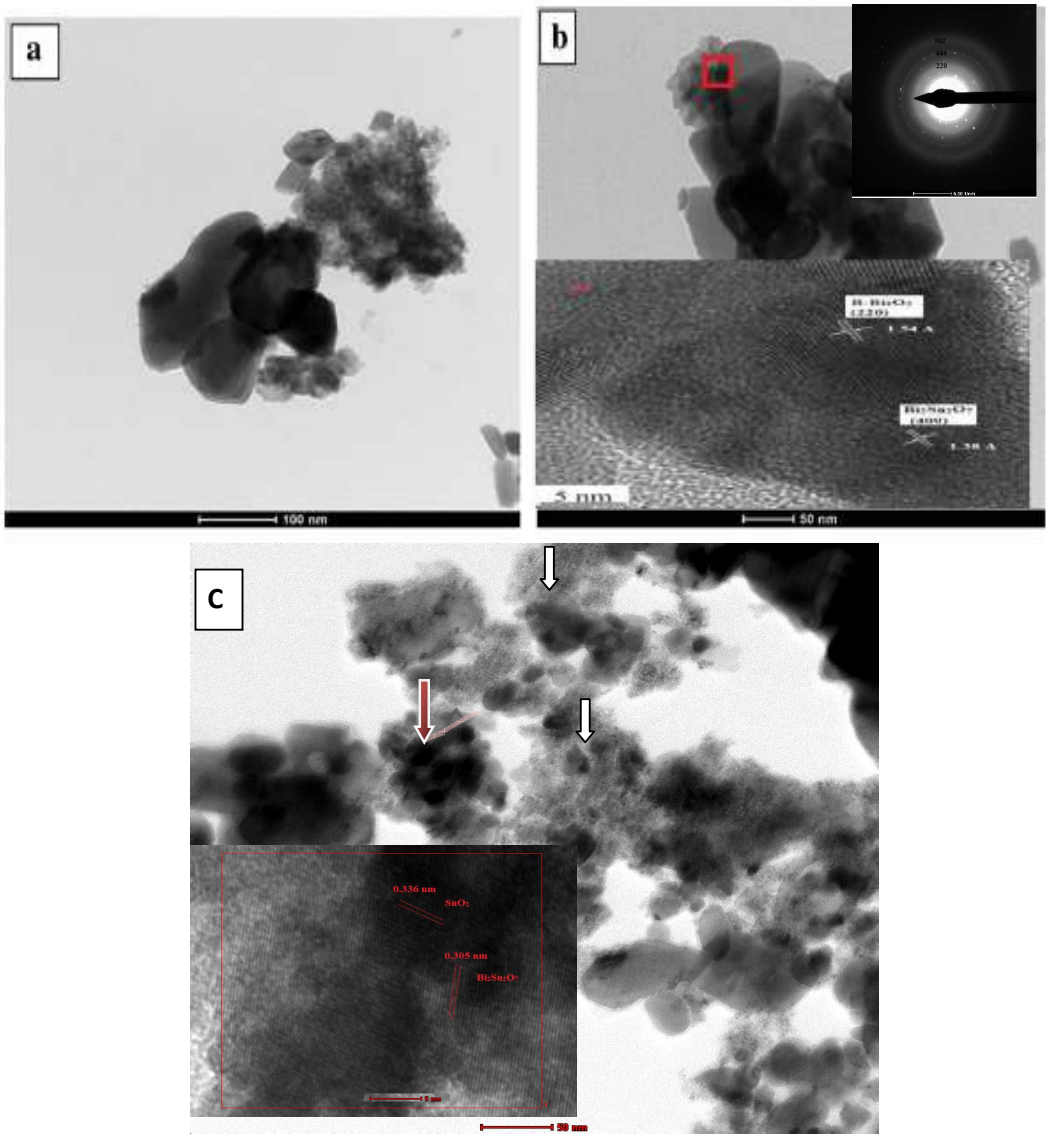


**Fig. 2**

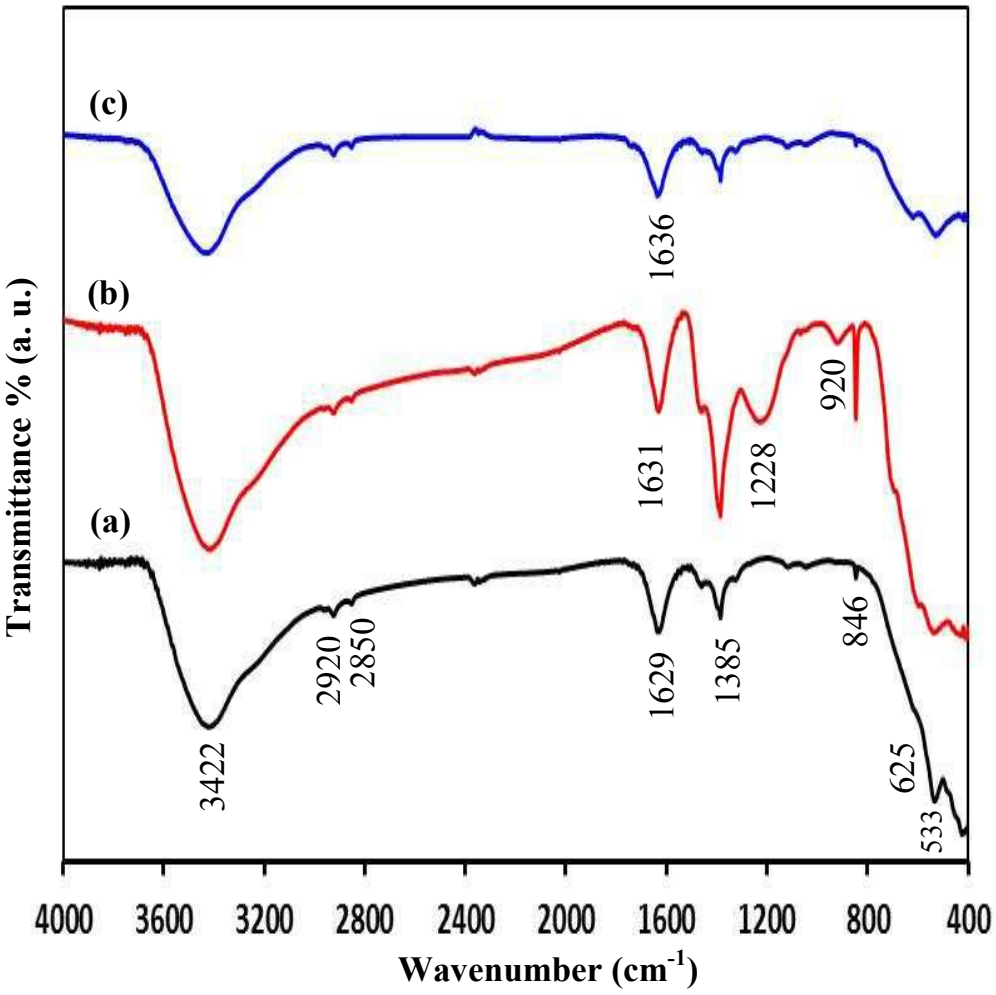


**Fig. 3**

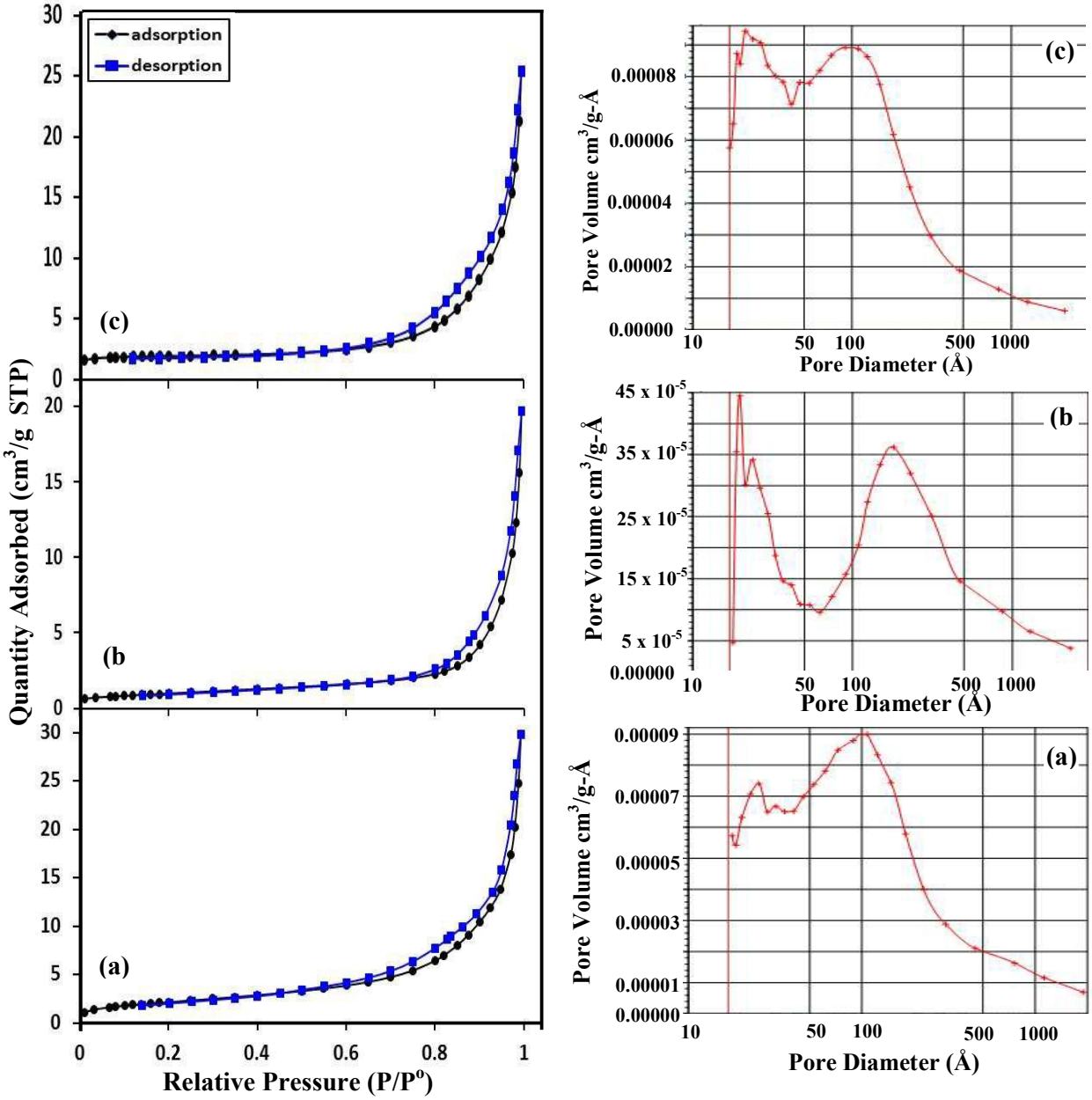


**Fig. 4:**

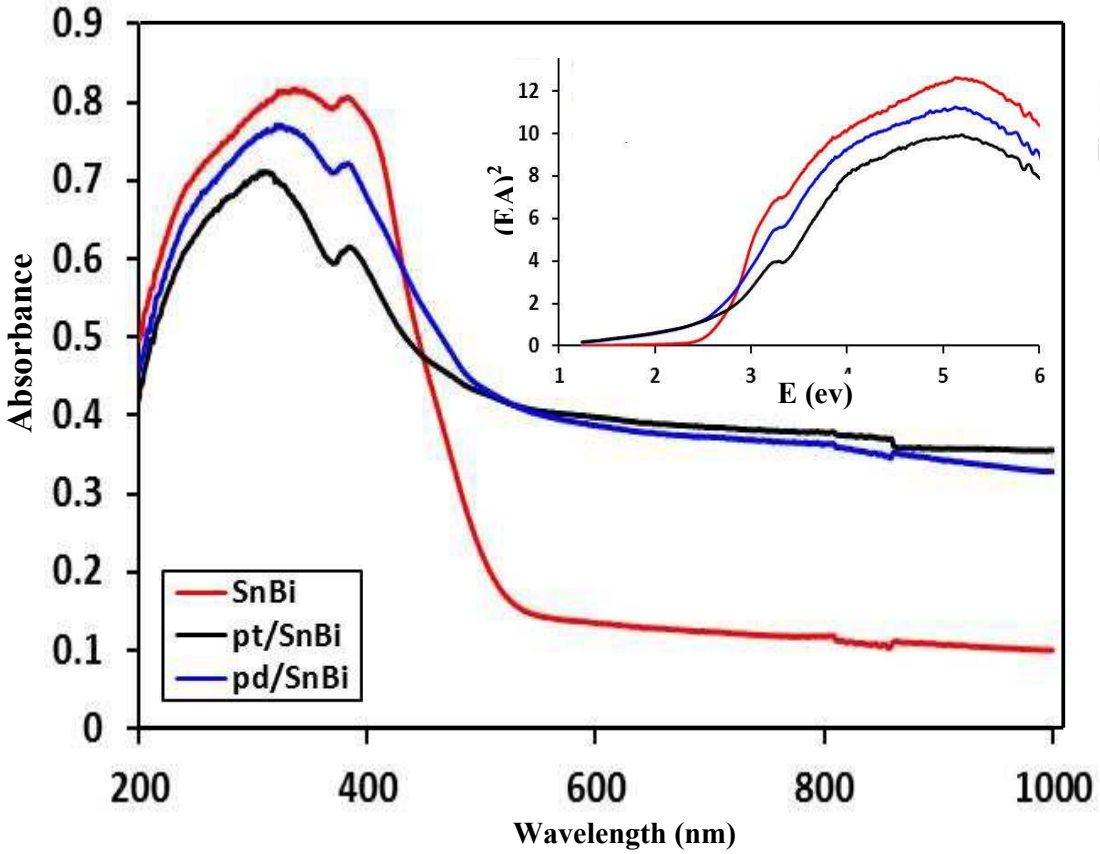


**Fig. 5**:

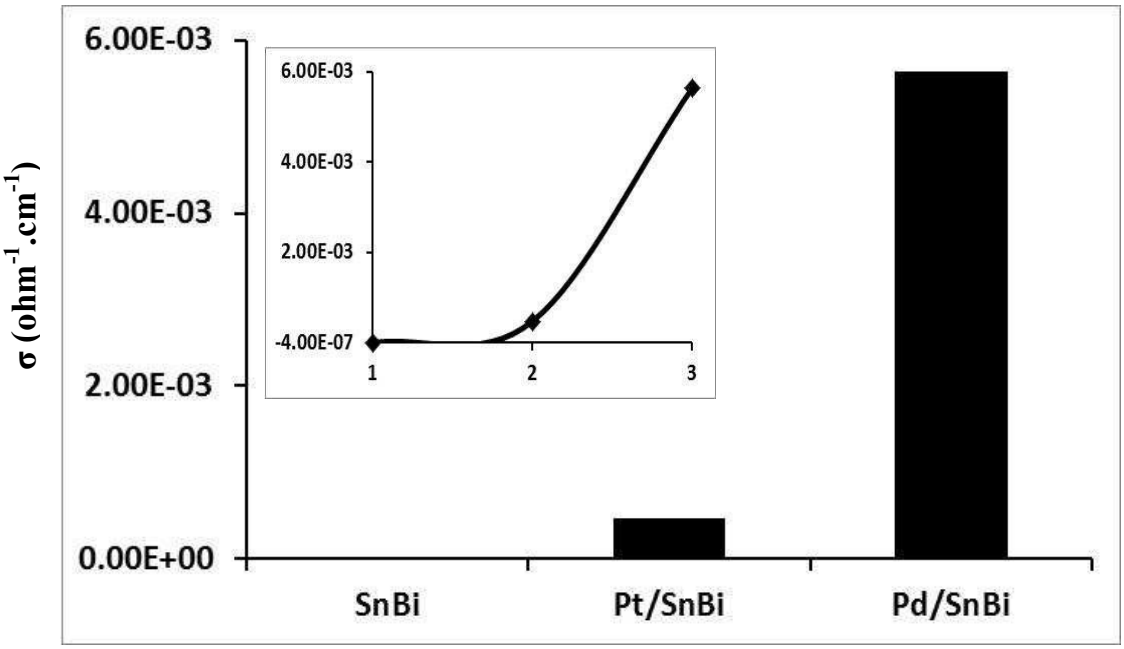


**Fig. 6:**

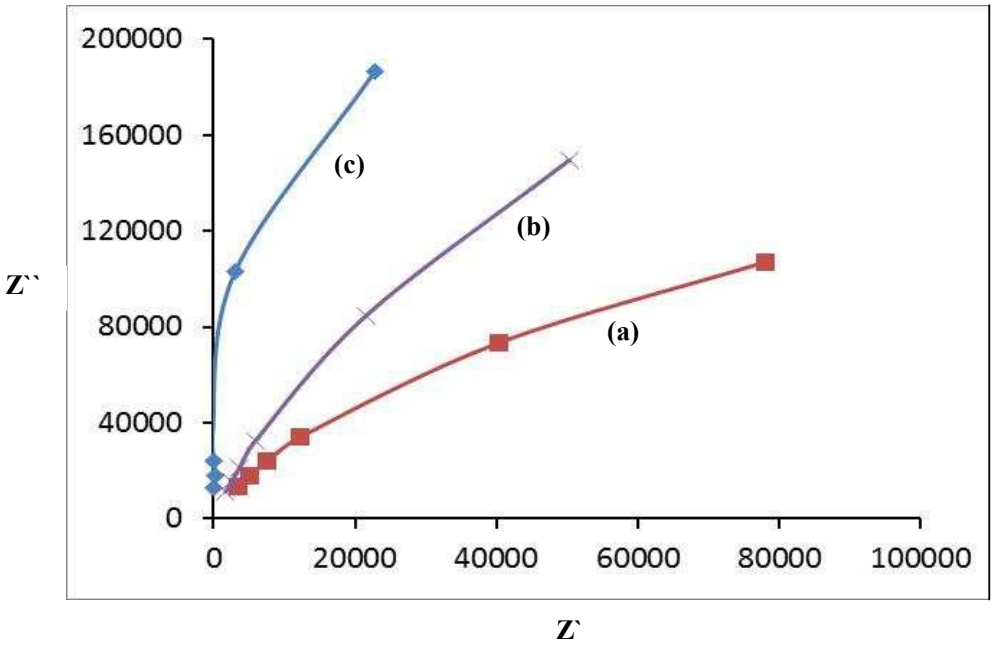


**Fig. 7:**

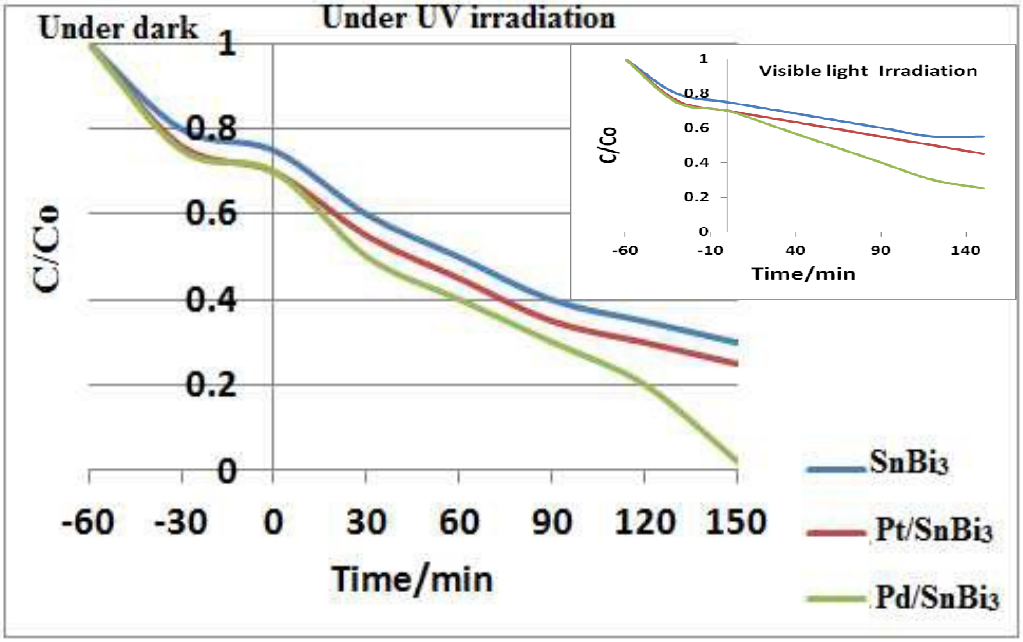


**Fig. 8**

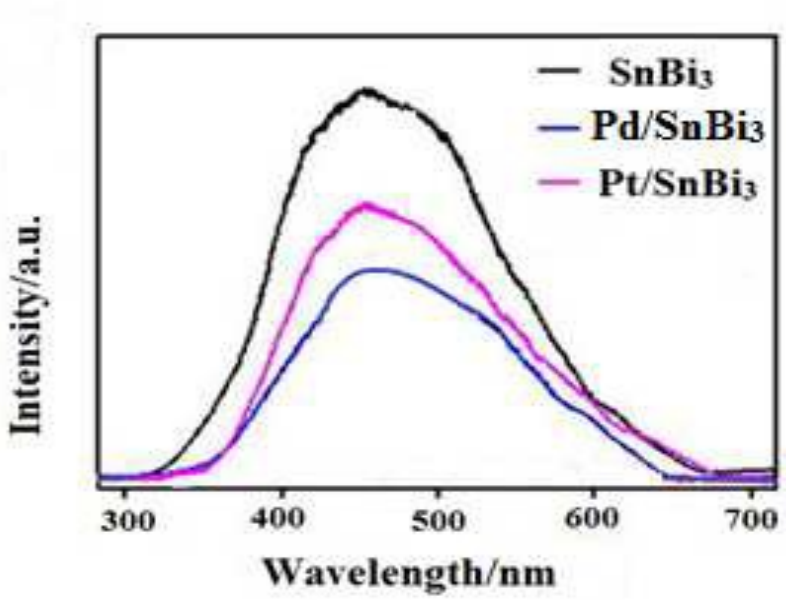


**Fig. 9**

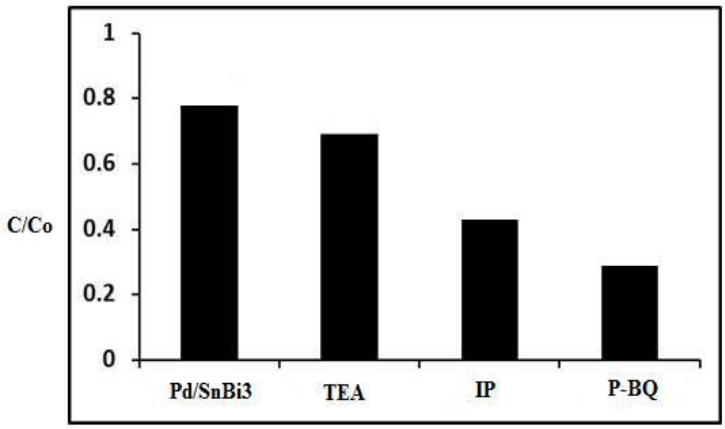


**Fig.10.**

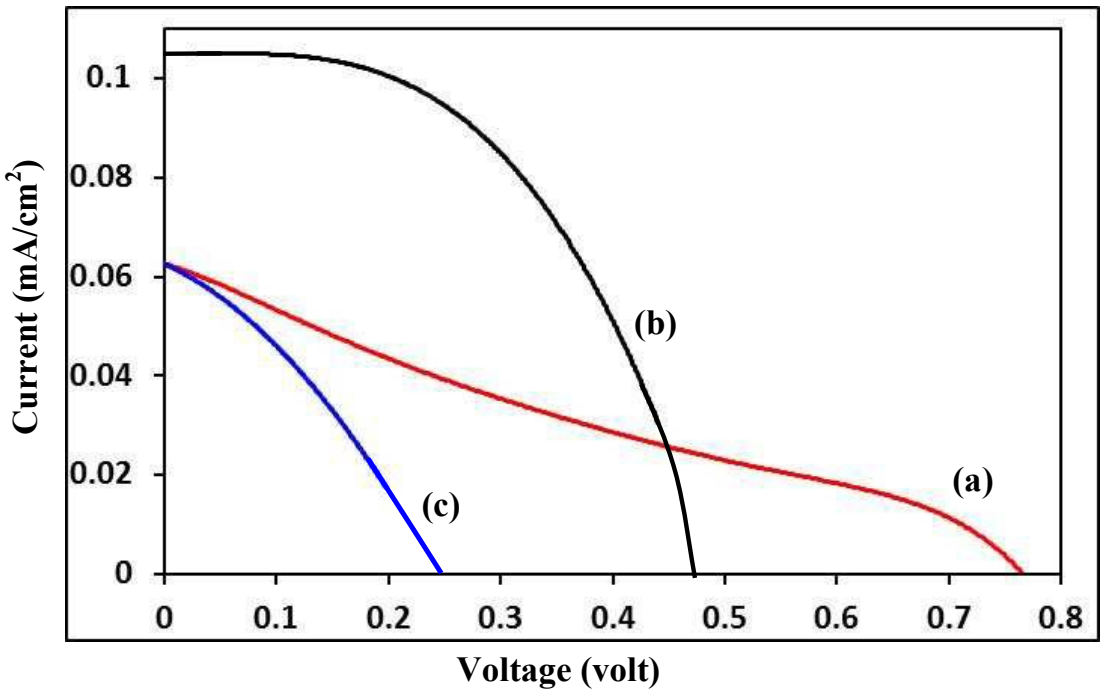


**Fig. 11**

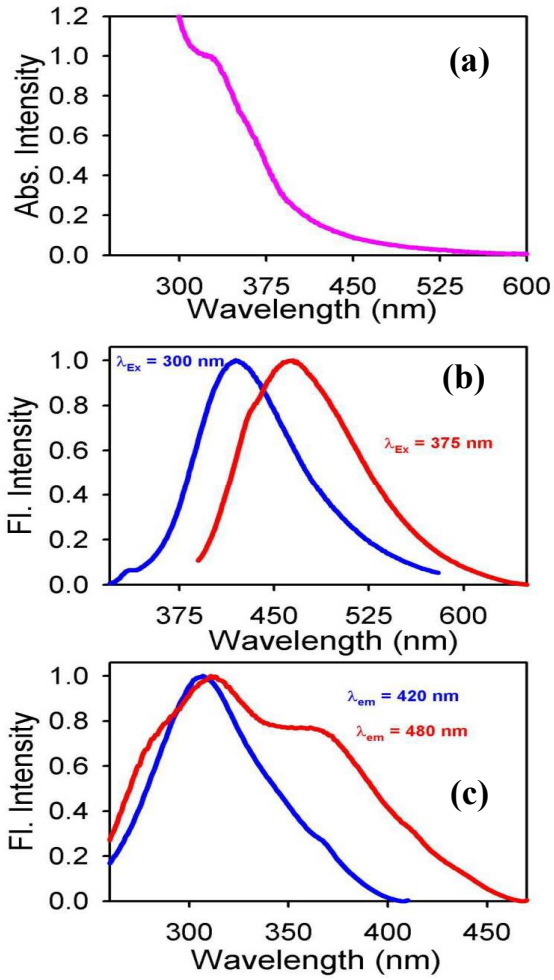


**Fig.12**

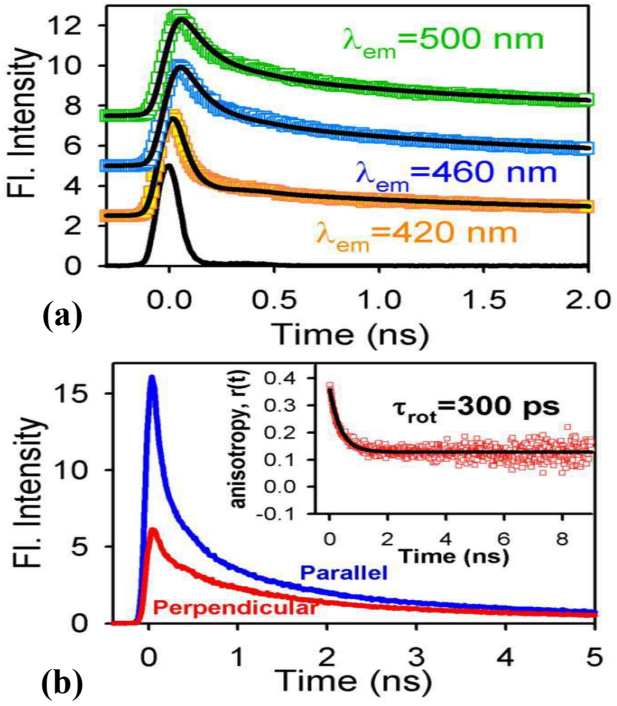


**Fig.13**

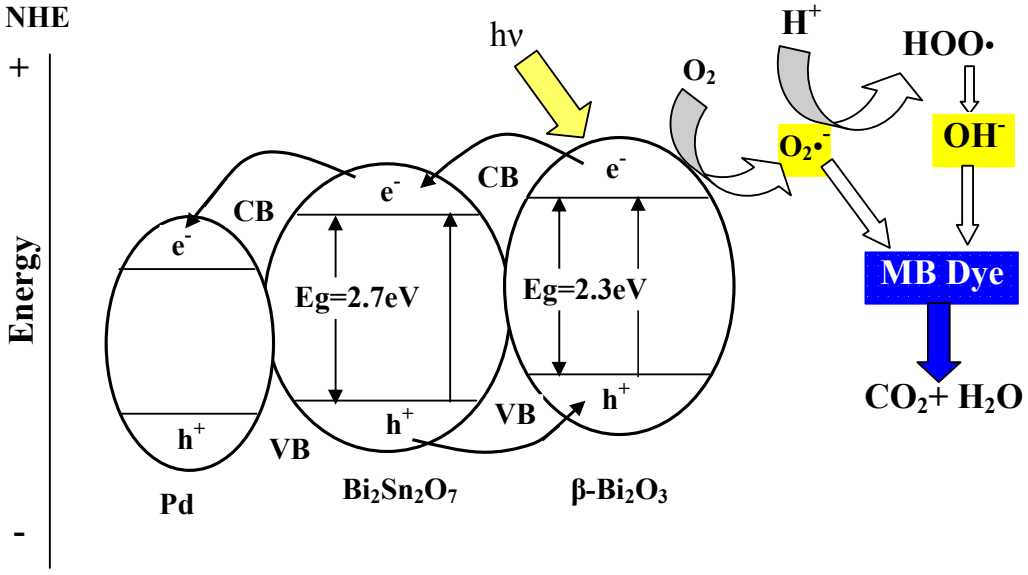


**Scheme 1.**